This is the accepted manuscript made available via CHORUS. The article has been published as:

Spin-polarized electronic states and atomic reconstructions at antiperovskite math xmlns="http://www.w3.org/1998/Math/MathML">mrow>msub>mi>Sr/mi>mn>3/mn>/msub>mi>Sn/mi>mi mathvariant="normal">O/mi>mrow>mo>(/mo>mn>001/mn>mo>)/mo>/mrow>/mrow>/math> polar surfaces

R. Arras, J. Gosteau, D. Huang, H. Nakamura, H. J. Zhao, C. Paillard, and L. Bellaiche

Phys. Rev. B **104**, 045411 — Published 12 July 2021

DOI: 10.1103/PhysRevB.104.045411

Spin-polarized electronic states and atomic reconstructions at the antiperovskite $Sr_3SnO(001)$ polar surfaces

R. Arras,[1] J. Gosteau,[1] D. Huang,[2] H. Nakamura,[3] H. J. Zhao,[3] C. Paillard,[4] and L. Bellaiche[3]

[1] *CEMES, Université de Toulouse, CNRS, UPS, 29 rue Jeanne Marvig, F-31055, Toulouse, France*
[2] *Max Planck Institute for Solid State Research, 70569, Stuttgart, Germany*
[3] *Physics Department and Institute for Nanoscience and Engineering University of Arkansas, Fayetteville, Arkansas 72701, USA*
[4] *Laboratoire SPMS, CentraleSupélec/CNRS UMR8580, Université Paris-Saclay, 8-10 rue Joliot-Curie, 91190 Gif-sur-Yvette, France*

We report a first-principles investigation of the atomic and electronic properties at the perfect and defective (001) surfaces of the antiperovskite Sr_3SnO. We first performed a thermodynamical study of the atomic structure terminations and demonstrated that SrSn-terminated surfaces should be the most stable one, either with a perfect (1×1) structure or with a (2×1) reconstruction induced by the formation of Sn vacancies. We detailed the surface gap states obtained for these surfaces, which we compare with those of other surface terminations, also having relatively low energies. These gap states, located near the Fermi level, could have a major contribution to the transport properties. Due to the lack of inversion symmetry associated with the surface, we predict that they also experience spin splittings, an important property for spinorbitronic applications. Finally, we found that Sr_2O-terminated surfaces could display a ferromagnetic ordering resulting from the population of $4d$ orbitals of Sr atoms at the surface and that this could lead to the formation of a spin-polarized two-dimensional electron gas.

I. INTRODUCTION

Antiperovskites, also known as inverse perovskites, possess the same crystallographic structure as normal perovskites, but with cations and anions having inverted their positions [1]. Following the fame of normal perovskite compounds and the increased richness of their interface and surface properties in nanostructures [2–4], it is now considered that studying antiperovskites could enable to enlarge again more the range of applications [5, 6] and of material candidates to display fundamental quantum properties, such as superconductivity [7] or topological electronic structures [8–10]. Understanding, functionalizing and optimizing these properties in a new class of materials requires extensive efforts to characterize their heterostructures and to develop an engineering of defects, surfaces and interfaces [11].

First-time grown in 1980 [12], Sr_3SnO is a good example of an antiperovskite that shows good promises. It has been predicted to be a 3D Dirac semimetal with a band structure having 6 Dirac cones along the Γ-X directions [13]. This material is formerly classified as a topological crystalline insulator [14, 15], that is, it displays surface states in the gap which are preserved by crystal inversion symmetry [16], or as a higher-order topological insulator displaying hinge states [17]. Recently, a superconducting behavior below a temperature $T \simeq 5$ K has been evidenced in Sr-deficient Sr_3SnO antiperovskites [18–20] and some hints of a ferromagnetic ordering have been attributed to the possible presence of oxygen vacancies [21].

Sr_3SnO possesses a perovskite structure with Sn^{4-} and O^{2-} anions occupying respectively cuboctahedral and octahedral atomic sites, formed by the sublattice of Sr^{2+} cations [22]. The anionic nature of Sn elements has been evidenced by Mssbauer spectroscopy in both stoichiometric and Sr-deficient Sr_3SnO compounds [20]. It has also been confirmed by x-ray photoelectron spectroscopy (XPS), while some signatures of neutral or cationic Sn atoms near the surface were also evidenced [22]. This finding can be related to the report of possible closely-neutral Sn ions in the vicinity of a Ca_3SnO surface [23].

The hypothetic $[Sr^{2+}]_3Sn^{4-}O^{2-}$ compound would display in consequences an alternation of $(SrSn)^{2-}$ and $(Sr_2O)^{2+}$ polar (001) atomic layers and a dipole moment normal to the surfaces, thus corresponding to surfaces of type 3, according to the classification proposed by Tasker [24]. Conserving the bulk structure, such a surface would be associated with the creation of an internal electric field and to the divergence of the electrostatic potential as a function of the film thickness, unless a charge transfer of ± 1 electron per formula unit is transferred to the surface [25]. It can thus be expected that growing $Sr_3SnO(001)$ thin films could lead to electronic reconstructions, on the basis of a polar catastrophe scenario [26, 27], or atomic reconstructions with the stabilization of structural defects such as vacancies. Due to the particular structure of antiperovskites and its predicted bulk band gap of a few tenths of meV, the properties of Sr_3SnO are expected to be very sensitive to the growth conditions and to its stoichiometry [20, 21]. Sr_3SnO and similar compounds have already been grown epitaxially on different substrates such as yttria-stabilized zirconia (YSZ)(001), $LaAlO_3(001)$, or even technologically-adapted substrates such as Si(001) using a YSZ buffer layer [21, 22, 28, 29]. To our knowledge, only (001)-oriented surfaces have been studied experimentally.

Concerning the theoretical studies on Sr_3SnO, most of them have been performed by combining first-principles calculations and tight-binding models in order to address the topological nature of this material [14, 15, 17]. These

works have however only considered ideal structures with perfect surfaces. More recently, the question of structural defects in the bulk crystal [30] and of perfect (001) surfaces [31] have been addressed separately and fully thanks to first-principles calculations.

To summarize, the surfaces of the antiperovskite Sr_3SnO, a candidate topological crystalline insulator, are polar surfaces for which the impact of possible electronic/chemical reconstructions on the protected surface states is not well understood. Those new surface structures could potentially lead to new ground states such as magnetic state, which has not previously been taken into account. Either conventional electronic reconstruction or magnetic transition could have a decisive effect on the true realization of surface states in these compounds. In consequence, we propose a detailed study based on *ab initio* calculations of the $Sr_3SnO(001)$ surfaces. We will first describe electronic reconstructions which appear at the perfect surfaces, with either a Sr_2O or a SrSn termination. The main properties of these surfaces will be compared with defective terminations in which vacancies or adatoms introduce atomic reconstructions and charge doping. A discussion of the relative stability of each surface termination is also provided.

II. CALCULATION DETAILS

We performed first-principles calculations based on the density functional theory (DFT) by using the Vienna *ab initio* software package (VASP) [32, 33]. We employed the projector augmented wave (PAW) method [34], a cut-off energy of 550 eV and the generalized-gradient approximation of the exchange-correlation energy proposed by Perdew, Burke and Ernzerhof and revised for solids (GGA-PBESol) [35].

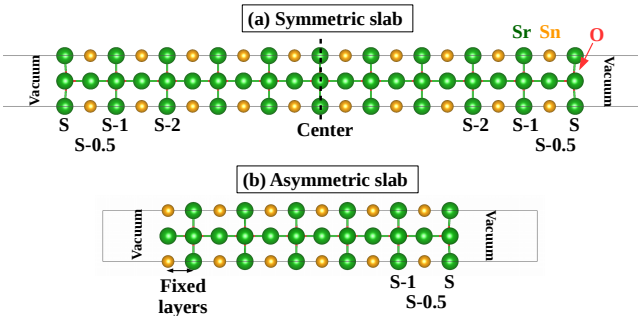

FIG. 1. (a) Symmetric and non-stoichiometric ($1 \times 1 \times 10.5$) slab with two non-equivalent Sr_2O-terminated surfaces and (b) Asymmetric and stoichiometric slab with a Sr_2O surface (S). The distance between the two atomic layers at the opposite surface is fixed to the bulk interplane distance.

As shown in Fig. 1, we performed direct calculations of the electronic properties of $Sr_3SnO(001)$ surfaces using different slab geometries and including a vacuum layer with a thickness of at least 15 Å to separate the two surfaces. These slab calculations can be compared to the calculations of bulk properties described in Appendix A. The in-plane lattice parameters have been fixed to the calculated bulk equilibrium value of $a_0(Sr_3SnO) = 5.1$ Å. Unless otherwise stated, the results presented in this paper have been obtained using more-convenient symmetric slabs, terminated by two equivalent surfaces and with a thickness of 21 atomic monolayers (MLs), that is 10 formula units (f.u.) of Sr_3SnO plus an added Sr_2O or SrSn ML (labeled 10.5 in the following). An example of such structure can be viewed in Fig. 1(a) for the case of a Sr_2O-terminated surface. Some differences obtained with such slab, if compared with an asymmetric slab, containing two non-equivalent surfaces [Fig. 1(b)], are also discussed throughout the paper, and more particularly detailed in Appendix B. We show in particular that, if the electronic reconstructions discussed in this paper have a different origin (off-stoichiometry or polar catastrophe) depending on the chosen geometry, they finally result in similar and robust surface states, with almost equal occupancy; only the symmetries induce noticeable changes, in the possibility that some bands will have to undergo spin-splitting lift of degeneracies.

The in-plane directions of the first Brillouin zone were sampled with a Monkhorst-Pack grid [36] of 15×15 vectors, for a supercell with 1×1 lateral dimensions.

Bader charges have been calculated using the Bader charge analysis code described in Ref. [37].

In the following, the (S) and (S−0.5) denominations correspond respectively to the surface and subsurface atomic monolayers (MLs). The labels $[Sr]_O$ and $[Sr]_{Sn}$ are given for Sr atoms located in a $Sr_2O(001)$ or SrSn(001) ML.

III. UNRECONSTRUCTED (001) SURFACES

In this section, we will describe the atomic and electronic structure of unreconstructed (001) surfaces of Sr_3SnO. For the calculations, we used symmetric $1 \times 1 \times 10.5$ slabs terminated by two equivalent surfaces with the ideal Sr_2O or SrSn termination, as shown in Fig. 1(a).

A. $Sr_2O(001)$-terminated surface

a. Atomic structure: At the Sr_2O-terminated surface, the interlayer distance is reduced to 2.43 Å between the surface (S) and subsurface (S−0.5) layers, *i.e.* by −4.7% if we compare with the bulk inter-atomic-layer distance of 2.55 Å. The calculated distortions then display oscillations in the following layers, with reduced magnitude (the interlayer distance is 2.59 Å (+1.4%) between the layers S−0.5 and S−1) up to the center of the slab, where we recover the bulk lattice parameter. Due to the different oxidation degree of each atom and the polar nature of Sr_3SnO, we also observe a cation-oxygen buckling along the z[001] direction, which is

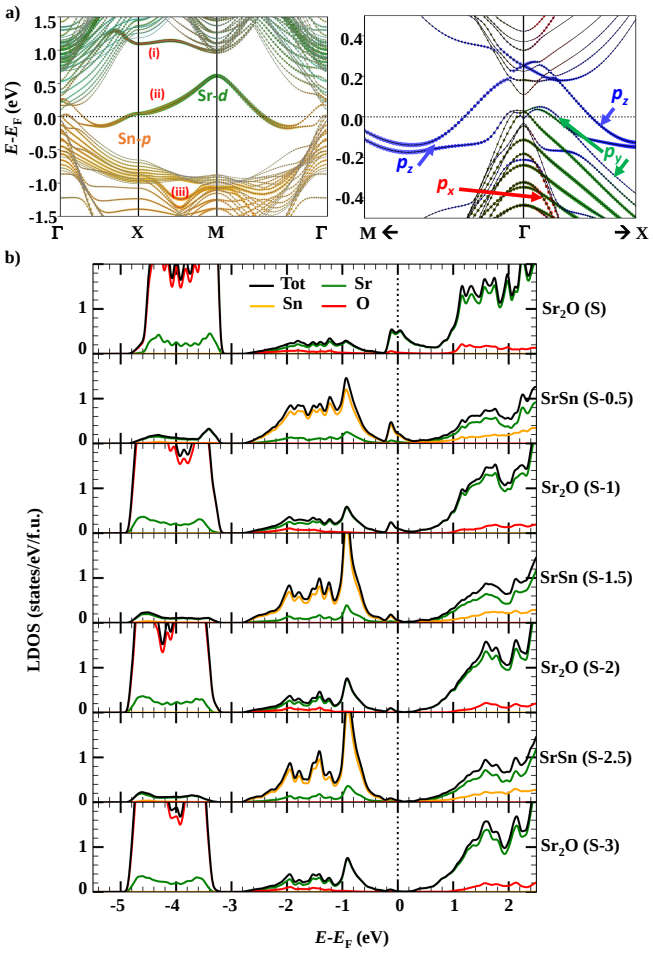

FIG. 2. (a) Band structure calculated with this same slab. The size of the colored circles is proportional to the contribution of each surface atom: On the left panel, the colors correspond to the $[\mathrm{Sr}]_{\mathrm{O}}$ (green), O (red), $[\mathrm{Sr}]_{\mathrm{Sn}}$ (cyan) and Sn (orange) atoms the nearest from the surfaces, while on the right pannel, we display a zoom with the detailed of the surface Sn-p bands contributions around the Γ point. (b) Layer-resolved densities of states (LDOS).

$\Delta z = \langle z(\text{cation})\rangle - \langle z(\text{anion})\rangle = 0.173$ Å at the surface layer. Such buckling is already 10 times smaller in the S−1 layer.

b. Electronic structure: The calculated band structure and the layer-resolved densities of states (LDOS) for the slab having a Sr_2O-terminated surface are given in Figs. 2(a) and 2(b). In the band structure, we can recover the bulk states forming parabolas centred around the Γ point, while the LDOS in atomic monolayers located in the center of the slab (starting from the layer (S-3)), are very similar to those of the bulk [see Fig. 11]. Clear gap states, labeled (ii) in the band structure, appear near the Fermi level. These gap states are expected to primarily participate to the conduction and it can be noticed that their intensity decreases when going toward the center of the slab, to reach an almost 0 value at the layer (S-3). The integration of the total DOS between $E_{\mathrm{F}} - 0.25$ eV and E_{F} is equal to 1.1 state, which will be occupied by electrons. Another surface state, labeled (i), can be observed around 1.2 eV above the Fermi energy, with a mix of $[\mathrm{Sr}]_{\mathrm{O}}$ and O character, while lower Sn-p states (iii), also with a strong surface contribution can finally be noticed below $E_{\mathrm{F}} - 1$ eV.

The following observations are also made.

First of all, p-d band anticrossings, appearing along the Γ-X direction in the bulk band structure [see Appendix A], are now located above the Fermi level. In the bulk, these crossings happen at the intersection between Sr-$d_{y^2-z^2}$ and Sn-$p_y + ip_z$ (for X of coordinates (0.5,0,0)) and they are generally associated with pseudo-Dirac points [13, 38, 39]. In the vicinity of a surface, they cannot be Dirac points, as the inversion symmetry would not be preserved anymore; their band character is moreover slightly changed, as, because of the surface, the y[010] and z[001] directions are also not equivalent, which consequently induces a lift of degeneracy of the p states.

The second interesting point is that the bands (ii), forming the surface gap states near the Fermi level, display a different band character as a function of the considered wave vector $\boldsymbol{k}$: These bands have mainly a Sr(S)-d_{xz},d_{yz} character between the X($\frac{1}{2}$,0,0) and M($\frac{1}{2}$,$\frac{1}{2}$,0) points, a Sn(S−0.5)-p_z near the Γ(0,0,0) point, and a mixed character otherwise. The two sets of bands corresponding to the surface states start changing their character around the X/2 and M/2 points, where these bands display a minimum. With this difference of orbital contributions, we also observe a different localization in real space. While these states between X and M are mostly unoccupied and possess a strong contribution coming from Sr atoms located in the surface layer (S), they tend to be more delocalized and they spread in the whole slab when having a Sn band character near the Γ point. This charge delocalization can be seen as a result of the p_z nature of the band and of the narrow band gap near Γ.

A third point is that, due to the position of the Fermi level, not only the aforementioned surface bands are crossing it, but also Sn-p_y bands, with a clear bulk nature, near the Γ point.

Finally, as it is shown in Appendix C, the band structure only slightly depends on the spin-orbit interaction, which only induces a small lift of degeneracy, splitting the surface states near the Fermi level into two sets of two non-spin-polarized bands around the X and M points.

c. Spin textures Still using a symmetric slab, we found out that, associated with the change of the orbital contributions of the surface states, we see a change of the spin orientation as a function of the wavevector $\boldsymbol{k}$: Always orientated in-plane, they are aligned along the [010] direction between X/2 and X and along the [100] direction along the X-M direction. For the symmetric slab, no spin splitting was observed. On the contrary, using an asymmetric slab, which lacks the inversion symmetry, as a real surface would, we observe such spin splittings in the band structures, as shown in Fig. 3, which give

spin textures consistent with a Rashba-like spin-orbit effect, with a dominant linear-in-$\boldsymbol{k}$ term around the X and M points (with spin vectors tangent to the energy contour) and a non-negligeable cubic character around the Γ point. The effective masses and splitting parameters calculated around the X and M points are given in Table II of Appendix B.

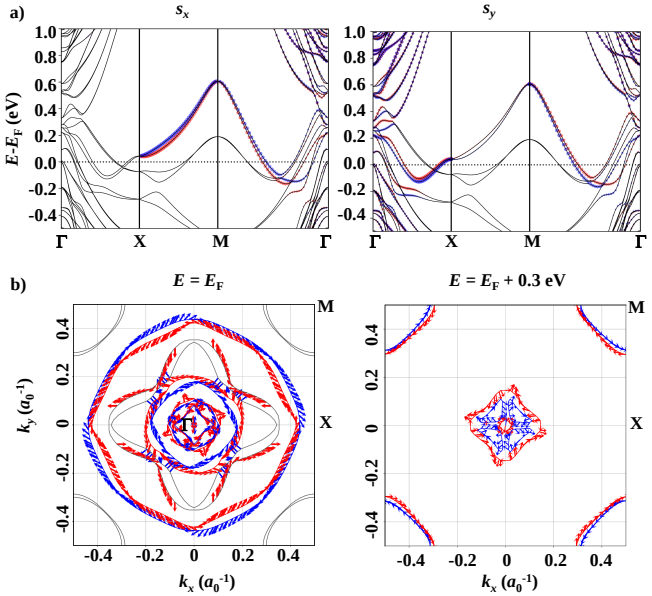

FIG. 3. Spin configurations at the Sr_2O-terminated surface as calculated with an asymmetric slab: (a) Spin-projected band structures and (b) iso-energy projections in the 2D 1st Brillouin zone, with the associated spin textures. Blue and red colors help to distinguish between the two splitted bands with opposite spin directions. Grey lines correspond to bands for which the atoms at the considered surface do not contribute.

d. Magnetic ordering: Up to now, we considered a perfect Sr_2O surface with the same nonmagnetic (NM) behavior as bulk Sr_3SnO compound. We also found it is possible to stabilize a ferromagnetic (FM) state, leading to the band structures shown in Figs 4(a) and 4(b); this FM state is more stable than the NM state, with an energy difference per surface f.u. $\Delta E = E_{\rm FM} - E_{\rm NM} = -0.43$ meV a_0^{-2}. We would like to mention that it was only possible to calculate the above-mentioned magnetic state by adding the spin-orbit interaction. Using the asymmetric slab, even in the absence of the spin-orbit interaction, we were able to recover a similar magnetic state, with a difference of total energy per surface f.u. separating the FM and NM state of $\Delta E = -1.42$ meV a_0^{-2}. From this observation, we can only infer the hypothesis that when the four surface bands, labeled (ii), are fully degenerate, a NM state is more stable, while lifting some degeneracy (using an asymmetric slab or adding the spin-orbit interaction) implies that fully occupying one set of two-bands by one charge of a given spin is more favorable, inducing in consequence the emergence of a ferromagnetic ordering.

For the symmetric slab, the corresponding total magnetic moment is orientated along the [111] direction, while it is along the [001] direction with the asymmetric slab. In both cases, it has a magnitude of 0.84 μ_B per surface f.u. The magnetic state appears to be a result of the charge reorganization, which results in the population of Sr-4d orbitals in the surface layer, as it can be seen in Figs 4(a) and Fig 4(c), in the case of a symmetric slab. The calculated total magnetic moment agrees with the redistribution of 2 electrons (one on each surface) resulting from the absence of a $(SrSn)^{2-}$ layer. As it can be seen in Fig. 4(c), the Sr-4d orbitals are not strongly localized near the atom nucleus and the spin density strongly extends in the vacuum; it results that the calculated spin magnetic moment calculated from the integration of states projected in the atomic sphere centered on a surface Sr atom is only 0.05 μ_B/atom.

Concerning the band structure, due to the magnetic exchange interaction, the ferromagnetic ordering leads to a band spin splitting which is of approximately 0.8 eV for $\boldsymbol{k}$ vectors for wavectors in the X-M direction, as it can be sen in Fig. 4(b). The band structure now displays bands crossing the Fermi level, which are linked to minority-spin electron pocket around the Γ point and to a majority-spin hole pocket around the M point.

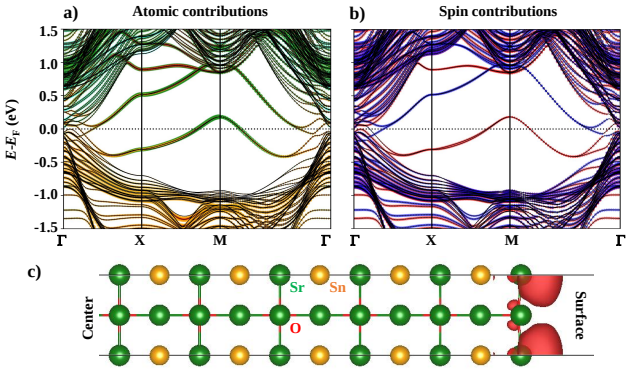

FIG. 4. Band structure of the perfect Sr_2O-terminated surface calculated with the spin-orbit interaction and for a magnetic state. a) The contribution of the atoms of the surface is given by the colored circles following the same color code than in Fig. 2. b) The sign of the spin projection s_z (with the quantization axis z along the [001] direction) on the band structure and c) the corresponding spin density is given in red for positive values and blue for negative values.

When the surfaces are in the FM states, the spin expectation values are orientated parallel to the total spin magnetic moment, *i.e.* along the [111] or [001] direction, respectively for the symmetric or asymmetric slab, showing a dominance of the magnetic exchange interaction over the spin-orbit effects. With the asymmetric slab, small values of spin projections, reminiscent of the spin-orbit-induced spin textures, can be observed along the x[100] and y[010] directions only for bulk bands, that are near the Γ point or at energies below $E_F - 1$ eV.

B. SrSn(001)-terminated surface

a. Atomic structure: The interlayer distance between the surface (S) and subsurface (S−0.5) monolayer is calculated to 2.46 Å, which corresponds to a reduction of −3.5%, that is lower than for the Sr_2O termination, on the contrary to an almost two-times larger cation-anion (Sr-Sn) buckling (+0.39 Å).

b. Electronic structure: Analyzing the electronic structure of the SrSn-terminated surface [Fig. 5], we can observe again the appearance of different surface gap states. These gap states more precisely correspond to depleting Sn-p states at the surface, which creates a band bending and a shift of the bulk peak, originally located at $E_F - 1$ eV, upward in energy, to the Fermi energy. From the LDOS, we can thus observe a peak of high density at the Fermi energy, resulting from bands with low dispersion. Around the Γ point, we indeed observe three sets of bands near the Fermi level, which correspond to Sn-p surface states. One of these sets of bands, labeled (i), stays close to the Fermi level and in the bulk band gap away of Γ; it possesses a majoritarily p_y character in the Γ-X direction, with a low dispersion, while it has a large p_z contribution along the directions X-M-Γ. The second set of band, which is more dispersive than the first one, possesses on the contrary a p_z, p_y and $p_x + p_y$ character, respectively along the Γ-X, X-M and M-Γ directions. The integration of the total DOS between E_F and $E_F + 0.4$ eV indicates the formation of 0.9 holes per surface, distributed approximately over five atomic layers.

Contrary to the NM Sr_2O surface for which the spin-orbit interaction leads to almost no visible effects on the electronic structure, it is important to note that for this surface termination, the band gap between the set of states (i) and (ii) at the X point is increased up to 0.2 eV as a direct result of the spin-orbit coupling. At this high-symmetry point, we thus observe an avoiding of the bands which is accompanied by a strong $p_y + p_z$ hybridization. Finally, the third set of bands, labeled (iii) and corresponding to Sn-p_x bands, displays a more dispersive behavior with a minimum at $E_F - 1.5$ eV at the X point. Both sets of bands (i) and (ii) cross the Fermi level in the Γ-X and Γ-M directions, while the set (i), the highest in energy and less occupied, displays a minimum at the X point, and a maximum, corresponding to a hole pocket at the M point, certainly resulting from the charge reorganization induced by the nonstoichiometry of the structure. In addition, it is also important to mention that for this surface termination, we only predict the appeance of an almost zero total spin magnetic moment of 0.04 μ_B per surface f.u. Using an asymmetric slab, it is possible to stabilize a magnetic state, but its origin certainly comes from the presence of the second and non-physical surface (with the Sr_2O termination), which is also primarily magnetized.

c. Spin textures As for the Sr_2O-terminated surface, the spins at the SrSn surface are orientated in-plane and along a direction perpendicular to the wavevector $\boldsymbol{k}$. Using an asymmetric slab induces the appearance of Rashba-like spin splittings, the values of which have been calculated using the spin-projected band structures of Fig. 6(a) and are given in Table II in Appendix B. We can notice that these values are of the same order of magnitude than for the other surface termination. Also similarly to the Sr_2O surface, we can see from the spin textures presented in Fig. 6(b) again mostly a linear Rashba behavior related to tangential spins around the X and M points, while cubic contributions are expected to be responsible of the deviation from this behavior near the Γ point. Large increase of the spin splitting can be noticed on the spin textures, for wavevectors for which the bands (i) and (ii) are the closest one from each other.

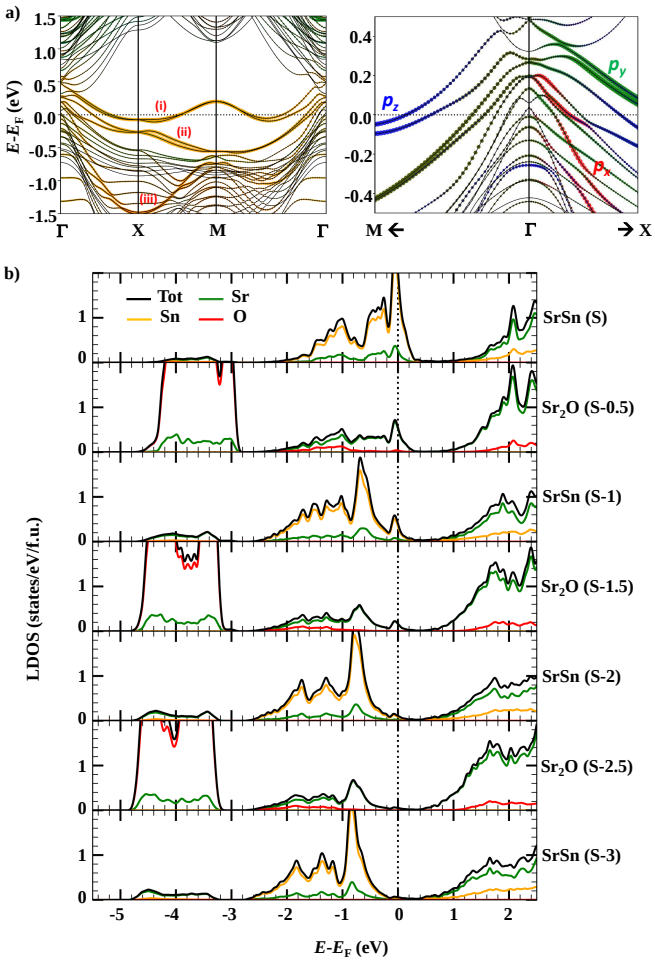

FIG. 5. (a) Band structure calculated for the SrSn-terminated surface. The size of the colored circles is proportional to the contribution of each surface atom: On the left panel, the colors correspond to the $[Sr]_O$ (green), O (red), $[Sr]_{Sn}$ (cyan) and Sn (orange) atoms the nearest from the surfaces, while on the right pannel, we display a zoom with the detailed of the surface Sn-p bands contributions around the Γ point. (b) Layer-resolved densities of states (LDOS).

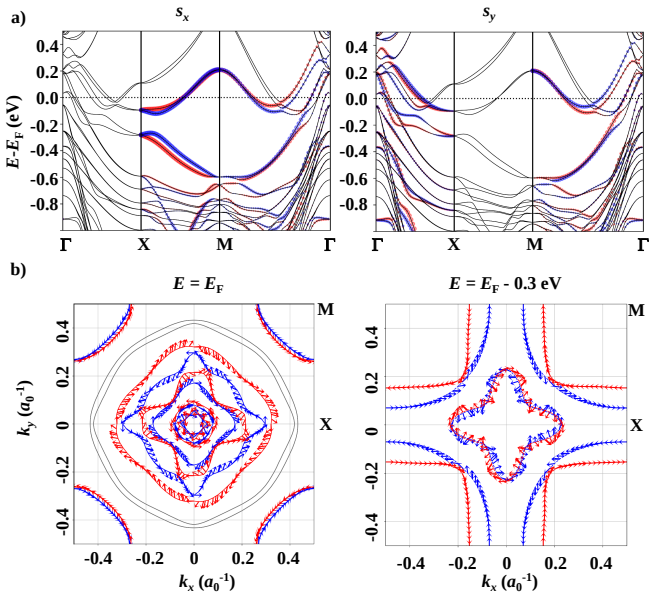

FIG. 6. Spin configurations at the SrSn-terminated surface as calculated with an asymmetric slab: (a) Spin-projected band structures and (b) Iso-energy projections in the 2D 1st Brillouin zone, with the associated spin textures. Blue and red colors help to distinguish between the two splitted bands with opposite spin directions. Grey lines correspond to bands for which the atoms at the considered surface do not contribute.

IV. RECONSTRUCTED (001) SURFACES

In the previous section, we considered perfect (001) surface terminations of Sr_3SnO, *i.e.* Sr_2O and SrSn, and we discussed the electronic modifications which appears in the vicinity of these surfaces. We will now verify which surface termination should be the most stable and if atomic reconstruction induced by the presence of point defects could be favored. When stable, we will describe the effects of these defects on the electronic and magnetic properties. The method to calculate the surface stability is explained in Appendix D. The properties described in this section have been calculated using $(2 \times 1 \times 10.5)$ slabs; as explained in Appendix D 3, as they were found more stable than $\left(\sqrt{2} \times \sqrt{2}\right)$R45°.

a. Stability of the surface terminations: The figure 7 gives the phase diagram of the surface termination stability as a function of the variations of the chemical potentials of Sr and Sn atoms. In a reasonable range of chemical potentials, we see that 5 different terminations can be stabilized. If we restrict ourselves to the chemical potentials fixed so that the bulk Sr_3SnO can be grown, we only have to consider the values matching with the dotted area in Fig. 7 [See Appendix D for more details]; in that case, we can first conclude that, according to our calculations, there is in principle a higher probability to obtain a SrSn-terminated surface, with potentially Sn vacancies (V_{Sn}), leading ultimately to a $SrSn_{0.5}$ surface (labeled "$SrSn+\frac{1}{2}V_{Sn}$"). The formation of Sr_2O-terminated surfaces, however, appear also realistic if we consider that their domain of stability are close to the limit of stability of the bulk and that our results may depend on the chosen exchange-correlation functional; in this latter case, we can see from Fig. 7 that the adsorption of oxygen atoms may lead to more stable $Sr_2O_{1.5}$ terminations (labeled "$Sr_2O+\frac{1}{2}O$") in oxygen-rich conditions.

To give a more quantitative idea of the energy differences between each surface termination, we can consider the averaged value of chemical potentials for which bulk Sr_3SnO is stable, *i.e.* the point of coordinates $\Delta\mu_{Sr} = -0.341$ eV, $\Delta\mu_{Sn} = -1.440$ eV, represented by a "+" sign in Figs. 7 and 15: With these values of chemical potentials, the energy difference between the perfect Sr_2O and SrSn terminated surfaces $\Delta\gamma_S = \gamma_{S=Sr_2O} - \gamma_{S=SrSn}$ is calculated to be almost 0 eV/surface formula unit and the calculated formation energy of a Sn vacancy at the SrSn surface is $E_d(V_{Sn}) = -0.21$ eV per defect [See Appendix D 3].

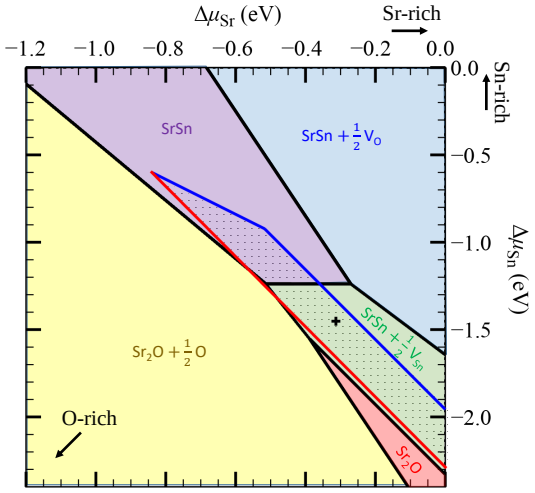

FIG. 7. Stability phase diagram for a $Sr_3SnO(001)$ surface. The dotted area corresponds to the domain of chemical potentials for which Sr_3SnO bulk can be synthetized [see Fig. 15 in Appendix D]. Each colored area corresponds to a chemical-potential domain for which a given surface termination is the most stable, *i.e.* displays the lowest surface energy γ_S as calculated using Eq. D5.

b. Induced atomic distortions: The introduction of a Sn vacancy at the SrSn-terminated surface does not change significantly the buckling, which is calculated to be 0.42 Å. Due to the unoccupied atomic sites created by the vacancy, we also observe an in-plane distortion, with a displacement of the surface Sr atoms away from the vacancy, by 0.38 Å along the x[100] direction. The buckling at the Sr_2O-terminated surface with an oxygen adatom is on the contrary strongly changed (-0.17 å) with an inversion of its sign. The atomic structures calculated for these two defective surfaces are shown in the

Appendix D 3 in Fig. 16.

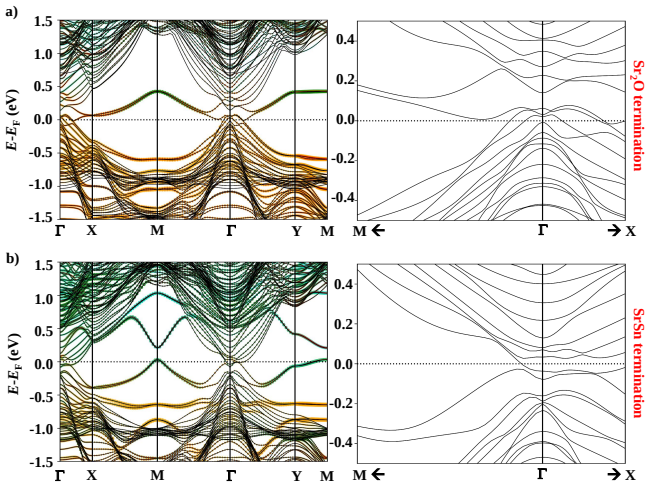

FIG. 8. Band structure of the most stable (2×1) defective surfaces, with (a) a $Sr_2O_{1.5}$ ($Sr_2O+\frac{1}{2}O$) termination or (b) a $SrSn_{0.5}$ ($SrSn+\frac{1}{2}V_{Sn}$) termination. The contributions of each atom of the surface are given by the colored circles following the same color code than in Fig. 2. A zoom of the band structures around the Γ point is given for each surface in the right panels.

c. Induced changes in the electronic structure: Figures 8(a) and 8(b) provide the band structures for the most stable (2×1) defective surfaces with respectively a $Sr_2O_{1.5}$ and $SrSn_{0.5}$ termination. The $Sr_2O_{1.5}$-terminated surface corresponds to a perfect (2×1) Sr_2O surface with an oxygen adatom located on top of one Sn atom. This surface displays a band structure very close to the one calculated for the perfect Sr_2O surface [Fig. 2(a)], except for the surface bands crossing the Fermi level for wavevectors closer from Γ in the Γ-Y and Γ-X directions, indicating that due to the presence of the additional negatively-charged oxygen ion, these bands tend to be less occupied. For this surface termination, it is also possible to note that the surface states near the Fermi level, which have mostly a Sn-*p* character for every surfaces, display a visible contribution from oxygen orbitals, as represented by the red circles.

If we now compare the defective $SrSn_{0.5}$-terminated surface [Fig. 8(b)] with its perfect counterpart [Fig. 5(a)], we can directly see that the surface states are strongly changed: This surface termination, certainly due to its Sn deficiency, indeed seems *a priori* to present more similarities with the Sr_2O termination. We can in particular highlight the set of bands crossing the Fermi level at the M point, forming a small hole pocket with Sr-*d* character. It is also intersting to note that around the Γ point, the bottom of the bulk conduction bands are crossing the Fermi level. We only calculated a total magnetic moment of 0.002 μ_B, which is not significant.

V. BADER CHARGES AND CORE-LEVEL ENERGIES

Experimentally, the surface electronic structure of $Sr_3SnO(001)$ has been investigated via ARPES [29] and XPS [22], both to map the band structure and to track the atomic valence states. Thus, in this section, we consider how the Bader charges and core-level energies (CLEs) are modified in perfect and reconstructed surfaces. These quantities are provided in Table I and will allow an analysis, complementary to the band structures described in Sections III and IV.

On the one hand, the formal oxidation states are obtained by subtracting calculated Bader charges to the number of electrons of the neutral Sr atom. Bader charge analysis [37] is one of the numerous methods which allow to obtain a numerical value of the charge carried by a chemical species [40] and this will help understanding the electronic reconstructions occuring in our systems. However, in practice, this method depends on a specific choice of partionning of the real-space volume and particular care has to be taken when comparing Bader charges of bulk and surface atoms. We chose to restrict the use of this method to the analysis of charge occupancy on Sr atoms, which possess sufficiently localized *d* orbitals and for which we calculated significant variations.

On the other hand, the CLEs are also sensitive to the local chemical and electrostatic environment and can be probed experimentally by XPS. The binding energy E_b associated with the removal of a core electron can be measured directly and, in the so-called initial-state approximation [41–43], it is equal to the opposite of the CLE ε_c, referenced to the Fermi level E_F:

$$E_b = -\varepsilon_c = -(\epsilon_c - E_F) \quad (1)$$

In Fig. 9 and Table I, we provide the variation in the Sn-3*d* CLE across the different layers, referenced to the value in bulk Sr_3SnO, *i.e.* $\Delta\varepsilon_{Sn,3d} = \varepsilon^{\text{layer}}_{Sn,3d} - \varepsilon^{\text{bulk}}_{Sn,3d}$. Overall, the CLEs do not deviate by more than a few hundred of meV from the value for anionic Sn in bulk Sr_3SnO, showing that anionic Sn remains stable and does not undergo a drastic change in valence state. Nevertheless, the small but systematic shifts in the Sn 3*d* CLEs across the different layers of the various slabs shed light on how charge is redistributed for the different surfaces. Similar to CLE shifts computed for surfaces of various transition metals [42], when small amounts of electrons (holes) are transferred to the Sn atoms, the extra potential rigidly shifts the valence DOS and core levels down (up) relative to the Fermi energy, thus increasing (decreasing) the CLE. We now describe the different surfaces in more details.

Fisrt, we can consider the perfect Sr_2O surface. From the band structure given in Fig. 2(a), we saw the presence of a partially-occupied surface gap state with a mixed character associated with Sn-*p* and Sr-*d* orbitals. This observation is in agreement with the decrease of the oxydation degree by 0.26 e of the Sr atoms located at the

TABLE I. Calculated properties of the $Sr_3SnO(001)$ surfaces: Surface and averaged core-level shifts $\Delta\varepsilon_{Sn,3d}$ and oxidation degrees estimated from the Bader charges for the Sr atoms in the surface layer. For a given defect, the calculated values are given for the structures with the lowest total energies [See Appendix D 3].

Structure	$\Delta\varepsilon^{S}_{Sn,3d}$ (eV)	$\langle\Delta\varepsilon_{Sn,3d}\rangle$ (eV)	$Q^{S}_{Bader}(Sr)$ (e)
Bulk			
Perfect	-	0	+1.24
Sr_2O termination			
Perfect (NM)	0.011	0.072	+0.98
Perfect (FM)	−0.098	−0.015	+1.08
$+\frac{1}{2}V_{Sr}$	0.154	0.097	+1.28
$+\frac{1}{2}V_{Sn}$	−0.269	−0.182	+0.81
$+\frac{1}{2}V_{O}$	−0.095	−0.046	+0.69
$+\frac{1}{2}O$	0.165	0.100	+1.14
SrSn termination			
Perfect	0.338	0.205	+1.30
$+\frac{1}{2}V_{Sr}$	0.438	0.250	+1.31
$+\frac{1}{2}V_{Sn}$	0.120	−0.054	+1.15
$+\frac{1}{2}V_{O}$	0.307	0.137	+1.26

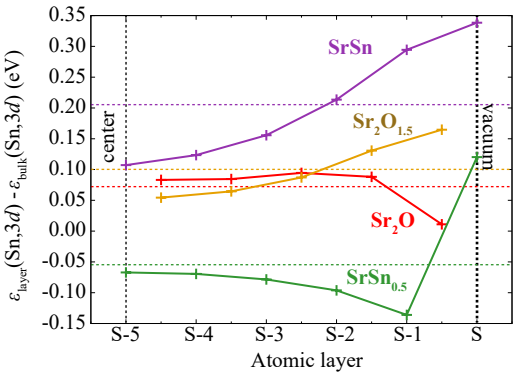

FIG. 9. Variation of the $3d$ core level energies $\varepsilon_{Sn,3d}$ as a function of the position of the Sn atom in regard to the surface layer (S). The colored dotted lines indicates the averaged CLS $\langle\varepsilon_{Sn,3d}\rangle$.

surface, as compared with the bulk, *i.e.* with an increase of the number of electrons, which will populate $4d$ orbitals of these atoms. From Fig. 9, we can also notice a decrease of the CLE $\varepsilon_{Sn,3d}$, that is the appearance of a band bending and a local internal electric field between the atomic layers "S" and "S-1.5", also indicating a transfer of electron to the Sn-p orbitals. The CLE for Sn atoms close to the center of the slab are tending toward an averaged value 72 meV higher than the bulk CLE; this is consistent with the band structure of Fig. 2(a), in which we can see that bulk states are above the Fermi level, which is itself pinned by the surface states. When turning to a magnetic state, the Sn-$3d$ CLE decrease by approximately 90 meV, mostly because of the lower lying partly-occupied surface state of majority spin.

Adding an oxygen atom at the (2×1) Sr_2O surface restores the bulk properties. It can indeed be seen that the calculated oxidation degree of the surface Sr atoms is +1.14 e, *i.e.* closer from the bulk value of +1.24 e. The averaged CLE, mostly representing bulk-like states, remains the same for this structure as for the perfect surface, while we can see an increase of the CLE for the subsurface atoms because of a shift of the Fermi level, which is consistent with a depopulation of the surface bands.

For the perfect SrSn termination, the charge balancing is obtained by distributing holes on Sn-p orbitals, which can be directly seen from the increase of the CLEs of the Sn atoms, while the oxidation degree of Sr atoms does not change significantly. Due to the less correlated nature of these bands, a part of these charges is localized near the surface, while the rest is spread over the whole slab. Because the SrSn surface is hole doped, while the Sr_2O surface is electron doped, we observe an internal electrical field which induces an opposite variation of the CLS [See Fig. 9].

For the three surface terminations described up-to-now, we saw that the charge reconstructions are mostly involving surface atoms, and the CLEs in the center of the slab are converging toward similar values (between 70 and 100 meV). The situation is different when Sn vacancies are present at the SrSn-terminated surface: While the CLE of Sn atoms at the surface is of 0.12 eV, it is well lower for every other Sn atom (in particular Sn atoms in the (S−1) layer) and the CLS of atoms in the center of the slab reach a value close to the average, *i.e.* −0.05 eV. The occupied d states at the M point observed in the band structure agree with the small diminution, by 0.1 e, of the Bader charge of the surface $[Sr]_{Sn}$ atom. This decrease is larger for the subsurface $[Sr]_O$ atoms: The oxidation degree is calculated to be +1.03 e, when averaged on all the 4 $[Sr]_O$ ions and it is −0.97 e if we consider only the two $[Sr]_O$ ions, first neighbors of the Sn vacancy.

To finish this analysis, we would like to point out that, ideally, $\Delta\varepsilon_{Sn,3d}$ should approach zero at the center of each slab, *i.e.* recover the bulk value. However, as we mentioned, there are differences ranging from 70 meV to 100 meV. The origin of these shifts is not easy to determine and it is difficult to rule out they can originate from methodological artifacts, because of the choice of the slab geometry and its limited thickness, for example. An explanation for the lowest value (−50 meV), calculated for the $SrSn_{0.5}$ surface termination, will be given in the next section.

VI. DISCUSSION

a. Stability of the surface terminations and atomic reconstructions: In their first-principles study, Bilal *et*

al. [31] already proposed, using another formalism, that a perfect SrSn(001)-terminated surface of Sr_3SnO is energetically more stable than a Sr_2O-terminated one. The authors also suggested that due to the small energy difference, both terminations could be present in polycrystalline samples. Our calculations confirm this prediction. Among the possible contributions, which would help minimizing the surface energy, we can note that the SrSn termination allows a higher cation-anion buckling. Such buckling results in the creation of electric dipoles partially cancelling the internal electric field close to the surface, which is a consequence of the charge discontinuity associated with the polar nature of Sr_3SnO(001). We also enlarged our study by considering the variations of chemical potentials, which can be related to experimental growth conditions, and by proposing simple surface reconstructions. We then found that a (2×1) $SrSn_{0.5}$ surface can be stable in Sn-poor conditions, which are still favorable to the growth of bulk Sr_3SnO. Finally, perfect or defectives Sr_2O-terminated surfaces could be obtained in oxygen-rich conditions.

Using the formula given in Ref. [22], it is possible to calculate core-level shifts (CLS) from the CLEs, which correspond, in this case, to the difference of binding energies between Sn-3*d* states in Sr_3SnO and in bulk α-Sn metal. For the $Sr_2O_{1.5}$ and $SrSn_{0.5}$ surfaces, CLSs are in agreement with the CLSs measured by XPS: Reported experimental values are -1.10 eV and -1.05 eV, while calculated values for Sn atoms in the surface layer, are -1.12 eV and -1.07 eV, respectively. This tends to validate our model and suggests that these surface terminations may be present in their studied samples, which would be an interesting point to verify. The experimental finding of neutral Sn atoms near the surface [22, 23] may indicate that other possible reconstructions could be present, leading to the formation of other compounds than the Sr_3SnO antiperovskite, like metallic Sn clusters.

b. Electronic reconstructions: Considering the four most probable surface terminations, *i.e.* Sr_2O, $Sr_2O_{1.5}$, SrSn and $SrSn_{0.5}$, we can now discuss the electronic reconstructions, associated with charge transfer and redistribution or to the presence of point defects. For the perfect surfaces, because we used an electrically-neutral and nonstoichiometric structure with two equivalent surfaces, either with a Sr_2O or a SrSn termination, respectively two electrons or holes are expected to be re-distributed inside the structure and to either spread in the entire slab by populating bulk bands, or to be equally localized at the two surfaces, leading to $(Sr_2O)^+$ or $(SrSn)^-$ terminations, this in order to preserve the electrical neutrality. A different mechanism involving charge transfer between the two different surfaces would settle if we used an asymmetric slab instead, but equivalent results are obtained for the perfect surfaces, as discussed in Appendix B.

For each surface, the main conclusions are summarized in Fig. 10 and explained below:

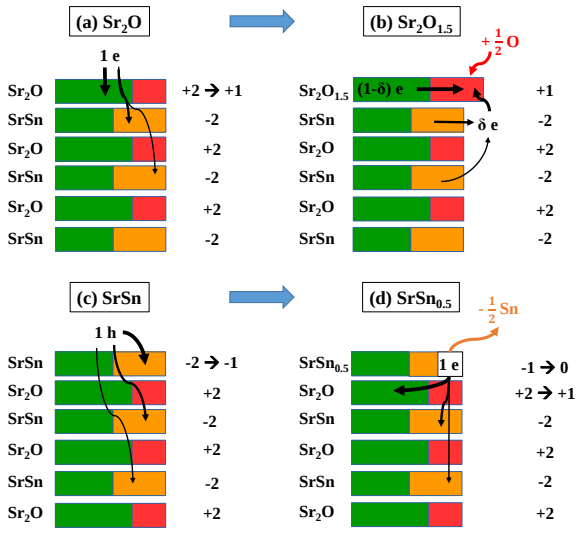

FIG. 10. Proposed diagrams showing the charge reconstruction at the four perfect or defective surfaces. The thickness of the arrows is approximately related to the amount of charges (electrons ("e") or holes ("h")) involved in the reorganization. The formal electric charges given on the right side of each atomic layers are approximated values before and after the electronic reconstruction (neglecting the charge extension away from the surface). The electronic reconstruction at the defective surfaces (b) and (d) may be explained relatively to the perfect surfaces (a) and (c). Green, orange and red squares represents the amount of Sr, Sn and O atoms. It is assumed that we consider a symmetric slab. Only a limited number of layers of a half of the slab is shown for the sake of simplicity.

1. In the case of the electron-doped *Sr_2O-terminated surfaces*, an extra electron per f.u. is partly localized at the surface and will mostly populate the partially-occupied gap states, as it can be seen in the DOS and band structures of Fig. 2. These surface bands have mostly a contribution coming from 4*d* orbitals of Sr atoms, as witnessed by the lower oxidation degree, but also of *p* orbitals of Sn atoms in further atomic layers. The electron localization in surface Sr-4*d* orbitals can lead to the stabilization of a magnetic state, with a total spin magnetic moment of 0.84 μ_B/surface f.u. As proposed in Fig. 10(a), in first approximation, that is, if we omit partial charges occupying some bulk Sn-*p* bands, the localization of the extra electron would then turn the $[Sr_2O]^{2+}$ surface layer into $[Sr_2O]^+$. The electron doping can originate from the off-stoichiometric structure or from a charge balancing between the polar surface and a second surface or an interface [See Appendix B]. This interesting feature could enable to generate spin-polarized two-dimensional electron gases (2DEG), owing to the relatively low effective masses we calculated [See Table II in Appendix B].

2. The *$Sr_2O_{1.5}$ surface*, in which an oxygen adatom is introduced, is energetically favorable for sam-

ples grown in oxygen-rich environment. This extra oxygen atom will transform into a negatively-charged O^{2-} ion by attracting two electrons. Such scenario may provide another way to preserve the electric neutrality and, in the same time, to add one electron per f.u. to the surface, without inducing charge transfer to the 4*d* bands of Sr atoms [See Fig. 10(b)]. This statement is confirmed by the Bader charge, which stays close to the one calculated for the bulk compound and also by the band structure which displays less occupied surface states. As it can be seen on the 3*d* CLE variation displayed in Fig. 9, a part of the charge attracted by the oxygen atom to form the O^{2-} anion is taken from the Sn bands, which are thus moving upward in energy. Surface bands of Sn-*p* orbital character also display an hybridization with the oxygen adatom orbitals, this one being located on top of one of the Sn atom from the subsurface layer.

3. The *SrSn surface* possesses a band structure with a hole pocket around the M point (with a strong contribution from Sn atoms at the surface layer), as shown in Fig. 5. The variations of CLEs show, however, that a part of the charge redistribution also affects Sn-*p* states deeper in the slab. This process is summarized in Fig. 10(c). Again if we make the omission of the extension of the surface state away from the surface, we can then conclude that the $[SrSn]^{2-}$ surface is hole-doped and turned into a $[SrSn]^{-}$ surface. According to our calculations, such surface could then host a quasi-two-dimensional hole gas (q2DHG).

4. Concerning the Sn-deficient $SrSn_{0.5}$ *surface*, the counting of the total formal charges leads to the conclusion that with the proposed symmetric slab geometry, we expect to have a redistribution of 1 electron per surface f.u., as for the perfect Sr_2O termination. The band structure in Fig. 8(b) shows indeed that one surface gap state is almost completely filled, suggesting some charge localization near the surface, with a mixed Sn-*p* and $[Sr]_O$-*d* character, as a function of the considered wavevector. First, it is important to note that the occupied Sr orbitals are those of Sr atoms of the subsurface layer (S-0.5) and not of the surface layer (S). The electronic reconstruction indeed does not involve the surface atomic layer, which is predicted to be electrically neutral, in agreement with the calculated value of the CLE of surface Sn ions (which is close from the averaged values calculated for the other surfaces). The band structure also shows that the bottom of the bulk conduction bands is crossing the Fermi level, inducing a total closure of the band gap at the Γ point, which would indicate that the remaining electron is transferred to the bulk. This occupation of bulk states is consistent with the calculated Sn CLEs in the center of the slab, which tends to a lower value in the center of the slab than the three other surfaces. In this scenario, both bulk and surface states are expected to participate to transport properties. As shown in Fig. 10(d), we thus propose a scenario in which the Sn vacancies at the surface are transferring charges mostly to the first-neighbor Sr_2O layer, but also partly to other inner layers.

To summarize, we proposed 4 different surfaces, 2 being hole-doped (with SrSn and $Sr_2O_{1.5}$ terminations) and the 2 others being electron-doped. For every interface, we observed clear surface states in the band gap of Sr_3SnO and which cross the Fermi level. These bands tend to spread away from the surface for wavevectors close to the Γ points, while they are associated with carriers more confined in the surface layer for wavevectors near the X and M points, in particular when they involve 4*d* orbitals. The characterization of such surface states as topological states would require a deeper analysis, which is beyond the scope of the present paper. We can however notice that the calculated states are crossing the Fermi level and are joining the bulk valence and conduction bands near the Γ point, as expected for topological states. These states may also look like projected states calculated with a DFT+tight-binding method by Chiu, *et al.* [15], who also predicted the possibility that such states would experience spin splittings. Finally, we showed that these lifts of degeneracies require the presence of the spin-orbit interaction, which is not the case for these surface states to exist, a property which has also been demonstrated in the case of topological crystalline insulators [16].

c. Magnetic state: An important point in our results is that we demonstrated that the 2DEG could be spin polarized, with the formation of a FM ordering. The stabilization of such magnetic ordering is consistent with earlier theoretical report of a magnetic state in Sn-deficient bulk Sr_3SnO [See Ref. [30] and Appendix D 3]; indeed, our symmetric slab with two equivalent Sr_2O surfaces also corresponds to a Sn-deficient structure with one missing SrSn(001) atomic layer. However, it is not probable that such ordering would remain at room temperature. It seems moreover clear from our calculations that it is not robust versus the presence of atomic defects or any change of the surface termination. More surprisingly, the $SrSn_{0.5}$ surface is also found to be nonmagnetic, while containing Sn vacancies, which may indicate a more complex physics, related with the fact that occupied Sr-*d* bands are located in the subsurface layer and not at the surface. Sr_3SnO is not the first d^0 oxides which would exhibit ferromagnetism, as other examples have been studied and the subject of debate for several years now. We can first cite the example of the famous $LaAlO_3/SrTiO_3$, in which a ferromagnetic state has first been evidenced in 2007 [44]. Some studies have suggested that it may result from the presence of localized 3*d* gap states induced by the presence of defects [45, 46]. If the exact origin of the magnetic ordering at this interface is subject to debate, it has been noticed both the TiO_2 and SrO interface ter-

minations can display ferromagnetism [47]. The physics of magnetic d^0 systems has often been compared with the establishment of ferromagnetism in diluted ferromagnetic semiconductors (DMS). Induced ferromagnetic ordering has been already reported or predicted in other dopant-free (*i.e.* without the addition of impurities) bulk materials such as TiO_2, $SrTiO_3$ or ZnO [48, 49], but also in compounds presenting less localized unoccupied $4d$ or $5d$ orbitals, such as α-PbO, In_2O_3, SnO_2, ZrO_2 or HfO_2 [49–56]: In general, the magnetic ordering is obtained by either changing the stoichiometry, by adding interstitials or vacancies, and/or by considering surfaces or confinement effects; while electron-doped materials result in partially filled d orbitals, filling oxygen p orbitals with holes may also induce ferromagnetism [50, 57]. The case of oxygen-deficient ZrO_2 is particularly interesting, as it has been shown that the ferromagnetic ordering was more likely to form in thin films or nanoparticles. Albanese, *et al.* [55] demonstrated that in nanoparticles the magnetic state only forms if the number of low-coordinated Zr atoms is sufficient in regard to the number of excess and available charges. They also found that the ferromagnetic ordering is favored by the hybridization between the gap states and the bands at the bottom of the conduction bands. Applied to our system, such explanation could match with our observations.

d. Other surfaces: Finally, even if other surface terminations are predicted to be less stable, we cannot discard that they could be obtained. It is important to keep in mind that growth mechanisms rely on out-of-equilibrium processes and that our calculated results are given for a specific exchange-correlation-energy functional. In addition, post-treatment like chemical treatments or post-annealing could be used to select a specific termination. In particular, we can mention the surface with a *SrSn termination and an oxygen vacancy* in the subsurface layer, which could be grown in oxygen-poor conditions, or the $Sr_{1.5}O$ termination, which possess *Sr vacancies* with a relatively low formation energy [See Table IV] and calculated CLSs ($\simeq -1.05$ eV) which also match with the above-mentionned experimental measurements [22]. Sr vacancies are particularly interesting because they are associated with the emergence of a superconductive behavior for a temperature below 5 K and resulting from hole doping. In their study, Oudah, *et al.* [18], proposed that Cooper pairs could have either a pure p-p orbital character or a mixed p-d character. According to our calculations, at least in the vicinity of a Sr-deficient surface, we expect the bands crossing the Fermi level and being doped by holes, to possess mostly a pure p character.

VII. CONCLUSION

To summarize, we performed a study, as complete as possible, of the $Sr_3SnO(001)$ surface states. We identified different surface terminations, which could be stable depending on the growth conditions, and we predict that SrSn-terminated surfaces are more likely to be obtained using suitable conditions for the growth of the Sr_3SnO antiperovskite.

We detailed the electronic properties of four terminations, which are the perfect Sr_2O and SrSn terminations and the (2×1) reconstructed $Sr_2O_{1.5}$ and $SrSn_{0.5}$ surfaces. Each surface displays clear gap states with a strong surface contribution around the X and M wavevectors, indicative of a two-dimensional carrier localization, which could lead to the emergence of a two-dimensional system. We found that electronic or atomic reconstruction favoring electron transfer to the surface induce the presence of mixed Sn-p and Sr-d states, while hole transfer implies that only pure p states will cross the Fermi level.

Finally, we found that in the case of a perfect Sr_2O termination, the surface could host a ferromagnetic ordering, due to the occupation of the Sr-$4d$ orbitals. This ordering is however not expected to be robust as we have shown that it can be destroyed by the addition of defects. On the contrary, the lack of spatial inversion symmetry induced by the surface, is suitable to the appearance of Rashba-like spin splittings, which could be another interesting feature of this interface, as it could be used in applications based on spin-to-charge current conversions.

ACKNOWLEDGMENTS

This study has been partially supported through the EUR Grant NanoX No. ANR-17-EURE-0009 in the framework of the *Programme des Investissements dAvenir*. H.J., C.P. and L.B. thank the Vannevar Bush Faculty Fellowship (VBFF) from the Department of Defense. This work was granted access to the HPC resources of CALMIP (Allocation No. 2020-2021/P1229).

Appendix A: Bulk calculations

The calculated equilibrium lattice parameter of the cubic bulk Sr_3SnO is $a_0(Sr_3SnO) = 5.10$ Å, *i.e.* -0.4% lower than the experimental parameter of 5.12 Å [12]. If the spin-orbit interaction is switched-off, the band structure of bulk Sr_3SnO shows that a band with a Sn-$p_y + ip_z$ character crosses the Fermi level in the Γ-X, Γ-M and Γ-R directions . As reported in Ref. [13] and shown in Fig. 11, when including the spin-orbit interaction, the band structure is gapped in the Γ-M and Γ-R directions and only two bands (omitting the spin degeneracy), with Sn-$p_y + ip_z$ and Sr-$d_{y^2-z^2}$ characters, are forming an anticrossing at the Fermi level in the Γ-X direction forming a pseudo-Dirac point. This anticrossing is characterized by the presence of a small band gap of 7 meV.

We also tested the influence of the exchange-correlation functional on the bulk electronic properties of Sr_3SnO. In Ref. [58], Vidal, *et al.*, warned that using standard DFT functional could lead to false positive

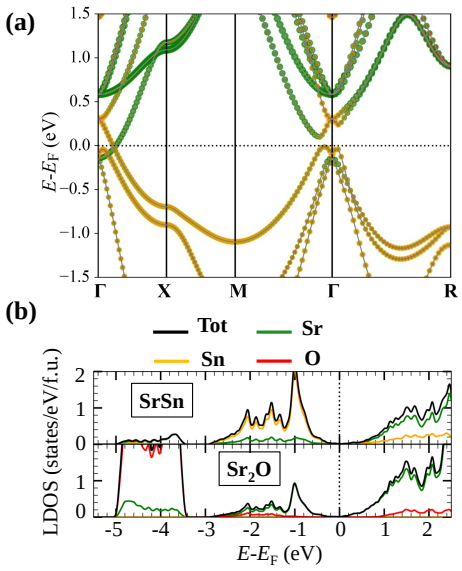

FIG. 11. Electronic structure of bulk Sr_3SnO calculated with the PBESol functional and the spin-orbit interaction: (a) Band structure for which the high-symmetry points have the coordinates $\Gamma(0,0,0)$, $X(\frac{1}{2},0,0)$, $M(\frac{1}{2},\frac{1}{2},0)$ and $R(\frac{1}{2},\frac{1}{2},\frac{1}{2})$, (b) LDOS. The contribution of each atom are highlighted with colors.

predictions of topological nature of some materials because of the underestimation of the band gap and the wrong determination of the relative energies between p and d bands. For this reason, we performed, for the bulk structure only, calculations using computationally more-demanding functionals. In the Γ-M direction, using the PBESol functional, we calculated a band gap width equal to 39 meV at the d-p antricrossing. We found that the semi-metallic character is preserved with other functionals, but the band gap is increased to 159 meV with the SCAN functional [59], and to 122 meV or 146 meV, using a PBESol+U [60] functional, with the U-dependent correction applied on the $4d$ bands of Sr atoms and $U = 1$ eV or $U = 2$ eV, respectively. Finally, when using the hybrid functional HSE06 [61], the band crossing is shifted toward the Γ point, which results in a closing of the band gap at this same point, this results is in agreement with the calculations reported in Ref. [14]. Unfortunately, the use of such functional is too time consuming to proceed to a more general comparison with surface calculations.

Appendix B: Dependence on the choice of the slab geometry

As explained in Section II, we proposed to describe mostly our results issued from calculations performed with a symmetric slab, *i.e.* formed with two equivalent surfaces. By construction, such a slab is non-stoichiometric, which may have consequences in particular for the study of polar materials. On the contrary, such geometry has the advantage to be able to consider only one interface at a time, which is convenient to compare the relative surface stabilities, but also to avoid artifactual atomic relaxations or charge transfers from a second interface, which is present using asymmetric slabs [See also the discussions in the supplemental material of Ref. [62]]. In this section, we will describe the main differences which can be expected regarding the choice of the geometry. To do so, in addition to the $(1 \times 1 \times 10.5)$ symmetric slab, we performed calculations using an asymmetric slab. The thickness of the new slab is of 6 layers of Sr_3SnO (12 atomic monolayers) along the z[001] direction. When optimizing the atomic structure, we fixed the positions of the atoms located in the two monolayers the nearest from one interface and let the positions of all other atoms relax.

By approximating the antiperovskite Sr_3SnO as a fully-ionic compound formed of Sr^{2+} cations and O^{2-} and Sn^{4-} anions, we expect the (001) layer to be polar and constituted of an alternation of $(Sr_2O)^{2+}$ and $(SrSn)^{2-}$ atomic layers. For an asymmetric film, with the combination of a SrSn and a Sr_2O surfaces, the polar character of Sr_3SnO leads to the appearance of an internal electric field for a thin film and an electronic reconstruction above a critical thickness following a polar catastrophe scenario, similarly to the processes proposed for polar-oxide-based heterostructures like the $LaAlO_3/SrTiO_3$(001) interface [26, 27]: Above a certain thickness, because of the electric-potential build-up associated with the internal electric field, the bottom of the conduction band and the top of the valence band, at each thin-film extremity, cross the Fermi level, causing a Zener breakdown, *i.e.* a charge balancing by tunnelling of electrons from the p-type to the n-type surface. This charge transfer is in particular necessary to avoid the divergence of the potential build-up as a function of the layer thickness. For Sr_3SnO, we can expect the transfer of 1 electron per formula unit (f.u.) from the $[SrSn]^{2-}$ to the $[Sr_2O]^{2+}$ surface, in order to cancel the potential build-up divergence; the band gap of Sr_3SnO being very low, the electronic reconstruction would be present for the lowest thickness.

In addition to the electronic reconstructions, other mechanisms have been proposed to explain the insulator-to-metal transition at polar interfaces, such as atomic reconstructions involving the formation of structural defects [46]. In the case of a symmetric slab, no internal electric field can appear between the two equivalent surfaces but the total atomic structure being non stoichiometric, the excess of positive or negative charges carried by the additional $[Sr_2O]^{2+}$ or $[SrSn]^{2-}$ atomic layer directly triggers the electronic reconstruction by redistributing the excess of positive or negative charges. This process would create surfaces carrying less, but non zero, electric charges, $[Sr_2O]^{+}$ or $[SrSn]^{-}$.

The mechanisms explaining the calculated charge redistribution are then different depending on the slab geometries, but the charge redistribution can be nonethe-

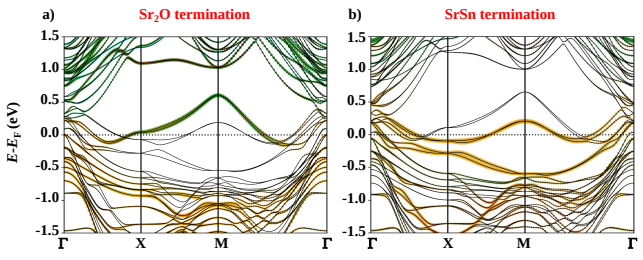

FIG. 12. Band structure calculated with the spin-orbit interaction for the (a) Sr_2-terminated and (b) SrSn-terminated surface. The same color code is applied as in Fig. 2. When comparing with the band structure of Fig. 2 and 5, we can see that additional bands appear, which are the result of the presence of the second, non-equivalent and non-physical, surface, for which the atomic layers are fixed to the bulk positions.

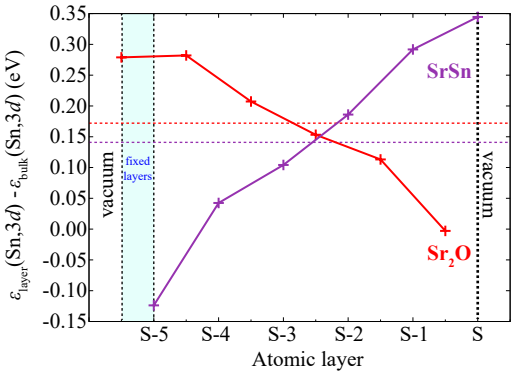

FIG. 13. Variation of the $3d$ core level energies $\varepsilon_{Sn,3d}$ as a function of the position of the Sn atom in regard to the surface layer (S). The colored dotted lines indicates the averaged CLE $\langle\varepsilon_{Sn,3d}\rangle$. These results have been calculated using asymmetric slabs; they can be directly compared with those obtained with symmetric slabs and displayed in Fig. 9.

less comparable for both configurations. As it can be seen by comparing Figs. 2(a) and 12(a) or Figs. 5(a) and 12(b), the band structures calculated for both geometries appear indeed similar; the crossing of the gap states with the Fermi level happens at almost the same values of wavevector for both structures and the band dispersions look similar, which suggests that an almost equal amount of charges is localized near the surface, independently of the chosen structure. This is confirmed by the Bader charges calculated for the Sr atoms located at the Sr_2O or SrSn-terminated surface, which are respectively 1.00 e or 1.26 e, in the asymmetric slabs. The CLE $\varepsilon^{S}_{Sn,3d}$ is also almost the same for both slabs at the surface, that is respectively 0.17 eV and 0.14 eV, while the average over the whole slab differs because of the second surface, which induces the presence of a residual internal electric field, as it can be seen in Fig. 13. The values of these internal electric fields $E_{\text{field}} = \frac{\delta\varepsilon_{Sn,3d}}{e\delta z}$, obtained by fitting the variation of CLE in the center of the slab, are -11 meV Å^{-1} and $+16$ meV Å^{-1}, respectively for the Sr_2O- and SrSn-terminated interfaces.

Beside the difference of stoichiometry, another question has to be addressed: It concerns the symmetries of our structures, in regard to the choice of slab geometry. This point is particularly important when considering spin-orbit effects. The bulk cubic perovskite structure possesses a $Pm\bar{3}m$ (No 221) space group associated with a O_h point group. When building the symmetric slab, the space group changes to $P4/mmm$ (No 123), with the fourfold rotation axis parallel to the normal to the (001) surface. Including a point defect on both surfaces with $\left(\sqrt{2}\times\sqrt{2}\right)$ dimensions [see Appendix D 3], does not change the space group, while using (2×1) dimensions makes x[100] and y[010] directions to become non-equivalent and reduces the space group to $Pmmm$ (No 47), with a two-fold rotation axis. Finally, asymetric slabs with perfect Sr_2O and SrSn surfaces will correspond to a $P4mm$ (No 99) space group, which does not possess neither the spacial inversion symmetry nor the m_{001} mirror symmetry. As already said, this lack of inversion symmetry, which would exist for real surfaces, allows the apparition of an internal electric field, but also of Rashba-like spin splittings in the band structure. Looking at the fine details of the band structures of Fig. 12, we can indeed notice many lifts of degeneracy, which can be associated with Rashba-like spin splittings, as it was shown in Figs. 3 and 6. We can see from these figures that the spin component is nul in directions parallel to the wavevector $\boldsymbol{k}$ and we also found it is zero in the z[001] direction, which is the polar axis (*i.e.* the normal to the surface): These features are characteristics of the Rashba effect. To characterize the energy spin splitting in a simple manner (without considering the point group), it is possible to fit the difference between the energy of the two bands of opposite spin $\Delta E_{\pm}$ as a function of the wavevector k by a third order polynom, such as $\Delta E_{\pm}(k) = a\cdot k + b\cdot k^3$ [63]. Around the M point of little point group C_{4v}, the coefficient a corresponds to the linear Rashba coefficient multiplied by a factor 2 and the cubic term b can be decomposed into two terms [namely γ' and γ'' in Ref. [64]]. The spin-splitting values fitted from our calculations around the X and M high-symmetry points are summarized in Table II. If the values of each coefficient remain modest, it can be noticed from the band structures that the spin splittings are enhanced in the vicinity of band anti-crossings. Interesting spin splittings can also be noticed near the Γ point, but due to the higher number of bands, mixing surface and bulk states, their analysis is more complex.

Appendix C: Effect of the spin-orbit interaction

In this section, we provide the band structures calculated for the two perfect surface terminations without the spin-orbit interaction; the band structures of Fig. 14 can be compared with those of Figs. 2(a) and 5(a) to

TABLE II. Effective masses m^* and spin splitting parameters a and b calculated for the bands of energy E, the closest from the Fermi level at the X and M points.

Direction	$E - E_F$ (eV)	m^* (m_0)	a (eV Å)	b (eV Å^3)
Sr_2O termination				
$X_{\to\Gamma}$	0.042	−0.54	0.10	−2.2
$X_{\to M}$	0.042	1.34	0.16	−1.6
$M_{\to X}$	0.606	−0.23	0.07	0
$M_{\to\Gamma}$	0.606	−0.33	0.08	−0.33
SrSn termination				
$X_{\to\Gamma}$	−0.077	4.04	0.04	0.47
$X_{\to M}$	−0.077	−2.03	0.21	−1.68
$M_{\to X}$	0.204	−0.69	0.05	−1.42
$M_{\to\Gamma}$	0.204	−0.88	0.05	−2.48

understand the effect of this interaction.

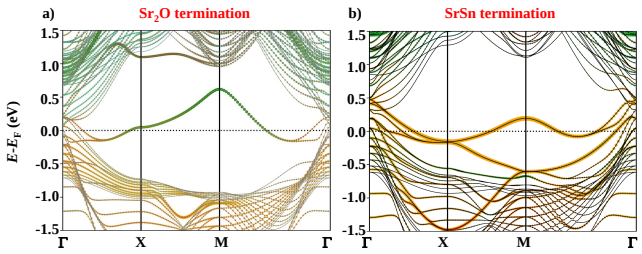

FIG. 14. Band structure calculated without the spin-orbit interaction for the (a) Sr_2-terminated and (b) SrSn-terminated surface. The same color code is applied as in Fig. 2.

Appendix D: Surface formation energy

The method used to calculate the surface formation energy [65, 66] consists in

1. defining the chemical potentials ranges for which the considered bulk compound is stable, in regard to all the other possible competitive phases,

2. searching for the most stable (001) surface terminations in the bulk stability range of chemical potentials, by comparing the enthalpies of formation.

This method is explained in the following for a general X_3YZ perovskite compound and then applied in the specific case of Sr_3SnO.

1. Enthalpy of formation of bulk Sr_3SnO antiperovskite

The enthalpy of formation $\Delta_f H$ of an antiperovskite of formula X_3YZ can be expressed as:

$$\Delta_f H\,(X_3YZ) = E^{\text{bulk}}_{X_3YZ} - \sum_i N_i E_i^{\text{bulk/gas}} \qquad \text{(D1)}$$

where $E^{\text{bulk}}_{X_3YZ}$ is the ground state total energy calculated for the X_2YZ antiperovskite, $E_i^{\text{bulk/gas}}$ are the total energies of the X, Y and Z atoms in their pure solid or gas phase and N_i are the number of atoms of each chemical specy. In the antiperovskite compound, the chemical potentials μ_i of these atoms may differ from $E_i^{\text{bulk/gas}}$ by an energy $\Delta\mu_i$, *i.e.* $\mu_i = E_i^{\text{bulk/gas}} + \Delta\mu_i$.

The conditions for the bulk antiperovskite to be stable are given by the following identity:

$$3\Delta\mu_X + \Delta\mu_Y + \Delta\mu_Z = \Delta_f H_B\,(X_3YZ) \qquad \text{(D2)}$$

with $\Delta_f H_B$ the formation enthalpy of the bulk antiperovskite, and by the following equations, which need to be verified in order to avoid any competitive phase to form:

$$n_x\Delta\mu_X + n_y\Delta\mu_Y + n_z\Delta\mu_Z \leq \Delta_f H_B\,(X_xY_yZ_z) \qquad \text{(D3)}$$

It is then possible to calculate a phase diagram, as proposed in Fig. 15, in which we can identify the couple of values of $(\Delta\mu_{Y=Sn}, \Delta\mu_{X=Sr})$ for which Sr_3SnO can be formed. In particular, knowing $\Delta_f H\,(Sr_3SnO)$ from Eq. D1, it is possible to notice that $\Delta\mu_O$ is always bound to $\Delta\mu_{Sr}$ and $\Delta\mu_{Sn}$ through the relation of Eq. D2. Moreover, the variation of chemical potential of the oxygen atoms $\Delta\mu_O$ can be related to the experimental growth conditions, *i.e.* the temperature T and the pressure P, using thermodynamical models as proposed in Refs. [66] and [67].

A first list of competitive phases has been established thanks to the *Materials project* database [68]; when several stable structures were reported for a given chemical composition, we selected the most stable one after a structural optimization performed keeping the same calculation parameters. The space groups are computed using the *FINDSYM* program [69, 70] with a tolerance of 10^{-3} Å applied on the atom coordinates and lattice parameters.

2. Surface energy

Considering a slab formed by a symmetric layer with two identical surfaces, we express the surface energy γ_S:

$$\gamma_S = \frac{1}{2A}\left[E_S - \sum_i N_i\mu_i\right] \qquad \text{(D4)}$$

with E_S the total energy of the slab of X_3YZ comporting two identical surfaces S of termination i and of area A. The chemical potentials μ_i are those calculated in the previous step, such as they are at equilibrium with the bulk.

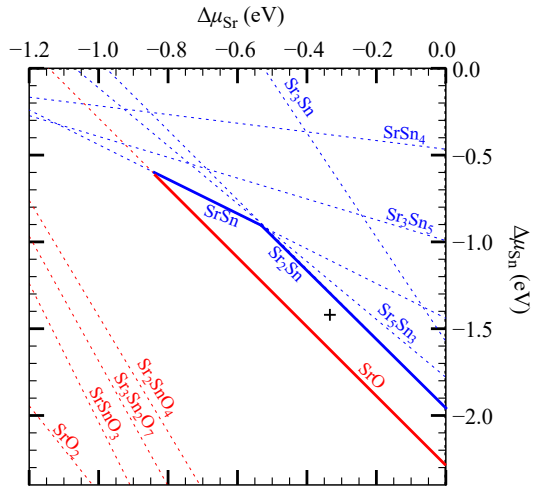

FIG. 15. Stability phase diagram of bulk Sr_3SnO oxide. Red and blue lines correspond to the constrain given by Eq. D3, blue and red colors means that Sr_3SnO is stable respectively below or above the given limit. This allows to define the stability domain delimited by the solid lines.

It is also convenient to reformulate Eq. D4 explicitely as a function of $(\Delta\mu_{Y=Sn}, \Delta\mu_{X=Sr})$, which for the study of Sr_3SnO surfaces gives:

$$\gamma_S = \frac{1}{2A}\left[\alpha + \beta\Delta\mu_{Sr} + \zeta\Delta\mu_{Sn}\right]$$
with
$$\alpha = E_S - \sum_{i=Sr,Sn,O} N_i E(i) - N_O \Delta_f H_B\,(Sr_3SnO) \quad \text{(D5)}$$
$$\beta = 3N_O - N_{Sr}$$
$$\zeta = N_O - N_{Sn}$$

By comparing the surface energy γ_S calculated for different surface terminations, it is possible to determine which atomic structure is the most stable for a selected couple of values $(\Delta\mu_{Y=Sn}, \Delta\mu_{X=Sr})$; interesting couples of values will be in particular those for which bulk Sr_3SnO is stable.

As mentioned in Refs. [71–73], calculating surface energies of polar oxides requires a lot of care and it is important to verify the convergence as a function of the vacuum and film thicknesses and of the $\boldsymbol{k}$ mesh used for the first Brillouin zone sampling, in order to ensure a good convergence of the energy as a function of the slab thickness (the reader can refer to Ref. [73] for more information about the different methods to circumvent such a problem). Performing our calculations, we verified that the 2D $\boldsymbol{k}$-mesh sampling used for the (001) slabs was matching with those used for the bulk calculations and we also checked that, by varying the slab thickness, we have a precision of 5 meV on the surface energy. Another critical point, which is standard in DFT calculations, arises from the choice of the exchange-correlation functional. In particular, it has been pointed out that the binding energy of the O_2 molecule may be overestimated [71, 72], which would justify the need to correct the chemical potential of oxygen atoms by shifting its value. If applying such correction would change the calculated formation energies of Sr_3SnO, the chemical potential of the oxygen atoms does not appear in the equation D5. Since different surface energies can display very close surface energies, depending on the growth conditions, we can in any case expect that different terminations will be present in real samples, explaining why we decided to compare different terminations.

3. Energy of defect formation

Another way to describe the previously mentioned surface terminations is to consider that they correspond to the association of a perfect surface termination with point defects. It is thus possible to define an energy of formation of the defect, which is expressed as a function of the energy of the slab or bulk supercell:

$$E_d = E_{sd} - \left(E_{sp} + \sum_i N_i\mu_i\right) \quad \text{(D6)}$$

with E_{sd} and E_{sp} the energies of the supercell respectively with and without the defect, and $\mu_i = E_i^{bulk/gas} + \Delta\mu_i$. With this new equation again, the formation energy E_d depends on the chosen values of the chemical potentials; taking the same averaged values as previously, we can then obtain the formation energies given in Table III and IV.

a. Formation of point defects in the bulk compound: We calculated the effect of vacancies in bulk supercells. The energies of formation, summarized in Table III, show that it is difficult to calculate an accurate energy for individual defects and that they strongly depend on the supercell size.

As calculated previously by Batool *et al.* [30], we found that a Sn vacancy induces the appearance of a ferromagnetic ordering by populating Sr-4*d* bands: We calculated a total magnetic moment of 1.04 μ_B, which is comparable to the value of 1.28 μ_B given in Ref. [30] and to the value calculated for the surface, *i.e.* 0.84 μ_B. This magnetic ordering is weak and is likely to be destroyed by the addition of defects at the surface. In the case of the bulk calculations, we found that it only appears for a very high content of vacancies, that is for the smallest supercell with $2 \times 2 \times 2$ dimensions.

b. Formation of defects at the surface: As seen in the previous paragraph, speaking of formation energy of a defect is not rigorous because of the high content of defects we considered; the concept of surface reconstruction is more adapted to this study. The formation energies given in Table IV, however, allows us to have an idea

TABLE III. Formation energies of defects E_d calculated using the values: $\Delta\mu_{Sr} = -0.341$ eV, $\Delta\mu_{Sn} = -1.440$ eV and $\Delta\mu_O = -5.484$ eV. For information, we also provide the averaged Sn-3d CLSs calculated with the $3 \times 3 \times 3$ supercells.

Surface dimension	Type of defect	E_d (eV/defect)	$\langle\Delta\varepsilon_{Sn,3d}\rangle$ (eV)
	Bulk		
$(2 \times 2 \times 2)$	V_{Sr}	0.22	
$(3 \times 3 \times 3)$	V_{Sr}	0.05	0.359
$(2 \times 2 \times 2)$	V_{Sn} (NM)	0.32	
$(3 \times 3 \times 3)$	V_{Sn}	0.09	−0.276
$(4 \times 4 \times 4)$	V_{Sn}	0.04	
$(2 \times 2 \times 2)$	V_O	0.15	
$(3 \times 3 \times 3)$	V_O	0.05	−0.066

of the energy difference separating the different surface terminations for a given set of chemical potentials.

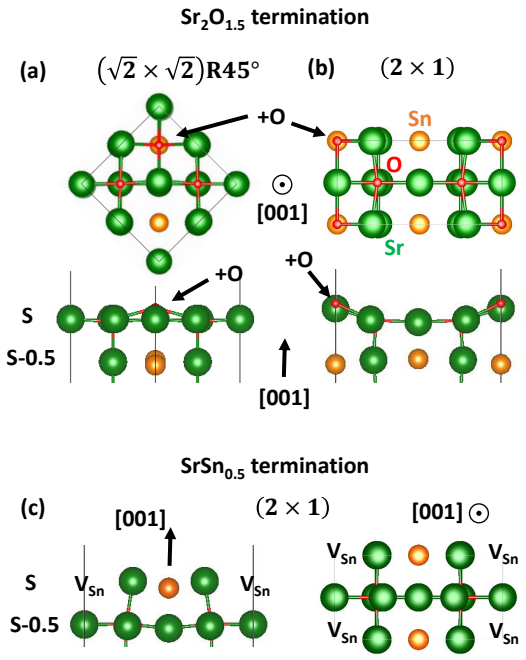

FIG. 16. Optimized atomic structure (side and top view) of the defective surface: (a) and (b) represent respectively the $(\sqrt{2} \times \sqrt{2})$R45°and (2×1) $Sr_2O_{1.5}$ surfaces, *i.e.* surfaces with a Sr_2O termination and an additional oxygen atom located in an interstitial position of the surface layer (S), (on top of a Sn atom from the subsurface layer (S−0.5)); (c) corresponds to a (2×1) SrSn surface with a Sn vacancy.

For the Sr_2O termination, we tested two different lateral dimensions to build our slabs: $(\sqrt{2} \times \sqrt{2})$R45° and (2×1). We can notice that the latter one gives almost systematically lower formation energies than the first one, which means that the (2×1) geometry gives more stable structures when including defects. This explains why we

TABLE IV. Formation energies of defects E_d at the $Sr_3SnO(001)$ surfaces. The calculations have been performed using Eq. D6 and with the variations of chemical potentials corresponding to the middle of the Sr_3SnO stability domain given by the black cross in Fig. 15, *i.e.* $\Delta\mu_{Sr} = -0.341$ eV, $\Delta\mu_{Sn} = -1.440$ eV and $\Delta\mu_O = -5.484$ eV. The defect "+O corresponds to an oxygen adatom located either in the surface layer (S) on top of the subsurface Sn atom, or initially on top (S+1) of a surface Sr atom. For the (2×1), there is two non-equivalent Sr atom (labeled "1" and "2"), which are respectively aligned with the oxygen atoms along the [010] and [100] directions (the [010] direction being twice shorter than the [100] direction, this may explain why the Sr1 vacancy is less stable than the Sr2 vacancy).

Surface dimension	Type of defect	location	E_d (eV/defect)
	SrO_2 termination		
$(\sqrt{2} \times \sqrt{2})$R45°	V_{Sr}	S	0.60
$(\sqrt{2} \times \sqrt{2})$R45°	V_{Sr}	S-0.5	1.28
$(\sqrt{2} \times \sqrt{2})$R45°	V_{Sn}	S-0.5	1.88
$(\sqrt{2} \times \sqrt{2})$R45°	V_O	S	0.61
$(\sqrt{2} \times \sqrt{2})$R45°	+O	S	0.40
$(\sqrt{2} \times \sqrt{2})$R45°	+O	S+1	4.14
(2×1)	V_{Sr1}	S	1.00
(2×1)	V_{Sr2}	S	0.40
(2×1)	V_{Sr}	S-0.5	0.99

[1] S. V. Krivovichev, Z. Kristallogr. **223**, 109 (2008).
[2] J. Mannhart and D. G. Schlom, Oxide interfaces—an opportunity for electronics, Science **327**, 1607 (2010).
[3] H. Y. Hwang, Y. Iwasa, M. Kawasaki, B. Keimer, and Y. Nagaosa, N. andTokura, Nature Mater. **11**, 103 (2012).
[4] The interface is still the device, Nature Mater. **11**, 10.1038/nmat3244.
[5] M. Bilal, S. Jalali-Asadabadi, R. Ahmad, and I. Ahmad, J. Chem. **2015**, 495131 (2015).
[6] Y. Wang, H. Zhang, J. Zhu, X. L, S. Li, R. Zou, and Y. Zhao, Adv. Mater. **32**, 1905007 (2020).
[7] T. He, Q. Huang, A. P. Ramirez, Y. Wang, K. A. Regan, N. Rogado, M. A. Hayward, M. K. Haas, J. S. Slusky, K. Inumara, H. W. Zandbergen, N. P. Ong, and R. J. Cava, Nature **411**, 54 (2001).
[8] Y. Sun, X.-Q. Chen, S. Yunoki, D. Li, and Y. Li, Phys. Rev. Lett. **105**, 216406 (2010).
[9] R. Yu, H. Weng, Z. Fang, X. Dai, and X. Hu, Phys. Rev. Lett. **115**, 036807 (2015).
[10] W. F. Goh and W. E. Pickett, Phys. Rev. B **97**, 035202 (2018).
[11] C. X. Quintela, K. Song, D.-F. Shao, L. Xie, T. Nan, T. R. Paudel, N. Campbell, X. Pan, T. Tybell, M. S. Rzchowski, E. Y. Tsymbal, S.-Y. Choi, and C.-B. Eom, Sci. Adv. **6**, 10.1126/sciadv.aba4017 (2020).
[12] A. Widera and H. Schfer, Mater. Res. Bull. **15**, 1805 (1980).
[13] H. Nakamura, D. Huang, J. Merz, E. Khalaf, P. Ostrovsky, A. Yaresko, D. Samal, and H. Takagi, Nature Commun. **11**, 1161 (2020).
[14] T. H. Hsieh, J. Liu, and L. Fu, Phys. Rev. B **90**, 081112 (2014).
[15] C.-K. Chiu, Y.-H. Chan, X. Li, Y. Nohara, and A. P. Schnyder, Phys. Rev. B **95**, 035151 (2017).
[16] L. Fu, Phys. Rev. Lett. **106**, 106802 (2011).
[17] Y. Fang and J. Cano, Phys. Rev. B **101**, 245110 (2020).
[18] M. Oudah, A. Ikeda, J. N. Hausmann, S. Yonezawa, T. Fukumoto, S. Kobayashi, M. Sato, and Y. Maeno, Nature Commun. **7**, 13617 (2016).
[19] J. N. Hausmann, M. Oudah, A. Ikeda, S. Yonezawa, and Y. Maeno, Supercond. Sci. Technol. **31**, 055012 (2018).
[20] M. Oudah, J. N. Hausmann, S. Kitao, A. Ikeda, S. Yonezawa, M. Seto, and Y. Maeno, Sci. Rep. **9**, 1831 (2019).
[21] Y. F. Lee, F. Wu, R. Kumar, F. Hunte, J. Schwartz, and J. Narayan, Appl. Phys. Lett. **103**, 112101 (2013).
[22] D. Huang, H. Nakamura, K. Küster, A. Yaresko, D. Samal, N. B. M. Schröter, V. N. Strocov, U. Starke, and H. Takagi, Phys. Rev. Materials **3**, 124203 (2019).
[23] M. Minohara, R. Yukawa, M. Kitamura, R. Kumai, Y. Murakami, and H. Kumigashira, J. Cryst. Growth **500**, 33 (2018).
[24] P. W. Tasker, The stability of ionic crystal surfaces, J. Phys. C: Solid State Phys. **12**, 4977 (1979).
[25] J. Goniakowski, F. Finocchi, and C. Noguera, Polarity of oxide surfaces and nanostructures, Rep. Prog. Phys. **71**, 016501 (2007).
[26] A. Ohtomo and H. Y. Hwang, Nature **427**, 423 (2004).
[27] A. Savoia, D. Paparo, P. Perna, Z. Ristic, M. Salluzzo, F. Miletto Granozio, U. Scotti di Uccio, C. Richter, S. Thiel, J. Mannhart, and L. Marrucci, Phys. Rev. B **80**, 075110 (2009).
[28] D. Samal, H. Nakamura, and H. Takagi, APL Mater. **4**, 076101 (2016).
[29] Y. Ma, A. Edgeton, H. Paik, B. D. Faeth, C. T. Parzyck, B. Pamuk, S.-L. Shang, Z.-K. Liu, K. M. Shen, D. G. Schlom, and C.-B. Eom, Adv. Mater. **32**, 2000809 (2020).
[30] J. Batool, S. M. Alay-e Abbas, A. Ali, K. Mahmood, S. Akhtar, and N. Amin, RSC Adv. **7**, 6880 (2017).
[31] M. Bilal, S. M. A. e Abbas, A. Laref, M. Noor, and N. Amin, J. Phys. Chem. Solids **136**, 109191 (2020).
[32] G. Kresse and J. Hafner, Phys. Rev. B **49**, 14251 (1994).
[33] G. Kresse and J. Furthmüller, Phys. Rev. B **54**, 11169 (1996).
[34] P. E. Blöchl, Phys. Rev. B **50**, 17953 (1994).
[35] G. I. Csonka, J. P. Perdew, A. Ruzsinszky, P. H. T. Philipsen, S. Lebègue, J. Paier, O. A. Vydrov, and J. G. Ángyán, Phys. Rev. B **79**, 155107 (2009).
[36] H. J. Monkhorst and J. D. Pack, Phys. Rev. B **13**, 5188 (1976).
[37] W. Tang, E. Sanville, and G. Henkelman, J. Phys. Condens. Matter **21**, 084204 (2009).
[38] T. Kariyado and M. Ogata, Journal of the Physical Society of Japan **80**, 083704 (2011).
[39] T. Kariyado and M. Ogata, J. Phys. Soc. Jpn. **81**, 064701 (2012).
[40] A. Walsh, A. A. Sokol, J. Buckeridge, D. O. Scanlon, and C. R. A. Catlow, Nature Mater. **17**, 958 (2018).
[41] W. Egelhoff, Core-level binding-energy shifts at surfaces and in solids, Surf. Sci. Rep. **6**, 253 (1987).
[42] M. Methfessel, D. Hennig, and M. Scheffler, Ab-initio calculations of the initial- and final-state effects on the surface core-level shift of transition metals, Surf. Sci. **287-288**, 785 (1993), proceedings of the 8th International Conference on Solid Surfaces.
[43] W. Olovsson, C. Gransson, T. Marten, and I. A. Abrikosov, Core-level shifts in complex metallic systems from first principle, Phys. Status Solidi (b) **243**, 2447 (2006).
[44] A. Brinkman, M. Huijben, M. van Zalk, J. Huijben, U. Zeitler, J. C. Maan, W. G. van der Wiel, G. Rijnders, D. H. A. Blank, and H. Hilgenkamp, Nature Mater. **6**, 493 (2007).
[45] N. Pavlenko, T. Kopp, E. Y. Tsymbal, G. A. Sawatzky, and J. Mannhart, Phys. Rev. B **85**, 020407 (2012).
[46] L. Yu and A. Zunger, Nature Commun. **5**, 5118 (2014).
[47] B. Kalisky, J. A. Bert, B. B. Klopfer, C. Bell, H. K. Sato, M. Hosoda, Y. Hikita, H. Y. Hwang, and K. A. Moler, Nature Commun. **3**, 922 (2012).
[48] B. Santara, P. K. Giri, K. Imakita, and M. Fujii, Nanoscale **5**, 5476 (2013).
[49] N. H. Hong, J. Sakai, N. Poirot, and V. Brizé, Phys. Rev. B **73**, 132404 (2006).
[50] G. Bouzerar and T. Ziman, Phys. Rev. Lett. **96**, 207602 (2006).
[51] N. H. Hong, N. Poirot, and J. Sakai, Phys. Rev. B **77**, 033205 (2008).
[52] S. Ning, P. Zhan, Q. Xie, Z. Li, and Z. Zhang, J. Phys. D: Appl. Phys. **46**, 445004 (2013).
[53] J. Berashevich and A. Reznik, Journal of Physics and Chemistry of Solids **75**, 1132 (2014).

[54] M. A. Rahman, S. Rout, J. P. Thomas, D. McGillivray, and K. T. Leung, J. Am. Chem. Soc. **138**, 11896 (2016).

[55] E. Albanese, A. Ruiz Puigdollers, and G. Pacchioni, ACS Omega **3**, 5301 (2018).

[56] K. Kalam, H. Seemen, M. Mikkor, P. Ritslaid, R. Stern, S. Dueñas, H. Castán, A. Tamm, and K. Kukli, ECS Journal of Solid State Science and Technology **7**, N117 (2018).

[57] M. Venkatesan, C. B. Fitzgerald, and J. M. D. Coey, Nature **430**, 630 (2004).

[58] J. Vidal, X. Zhang, L. Yu, J.-W. Luo, and A. Zunger, Phys. Rev. B **84**, 041109 (2011).

[59] J. Sun, A. Ruzsinszky, and J. P. Perdew, Phys. Rev. Lett. **115**, 036402 (2015).

[60] S. L. Dudarev, G. A. Botton, S. Y. Savrasov, C. J. Humphreys, and A. P. Sutton, Phys. Rev. B **57**, 1505 (1998).

[61] J. Heyd, G. E. Scuseria, and M. Ernzerhof, J. Chem. Phys. **124**, 219906 (2006).

[62] M. Stengel, Phys. Rev. Lett. **106**, 136803 (2011).

[63] J. Gosteau, R. Arras, P. Chen, H. J. Zhao, C. Paillard, and L. Bellaiche, Phys. Rev. B **103**, 024416 (2021).

[64] R. Arras, J. Gosteau, H. J. Zhao, C. Paillard, Y. Yang, and L. Bellaiche, Phys. Rev. B **100**, 174415 (2019).

[65] K. Reuter and M. Scheffler, Phys. Rev. B **65**, 035406 (2001).

[66] E. Heifets, E. A. Kotomin, Y. A. Mastrikov, S. Piskunov, and J. Maier, Thermodynamics - interaction studies - solids, liquids and gases (InTech, 2011) Chap. Thermodynamics of ABO_3-type perovskite surfaces.

[67] J. Osorio-Guillén, S. Lany, S. V. Barabash, and A. Zunger, Phys. Rev. Lett. **96**, 107203 (2006).

[68] A. Jain, S. P. Ong, G. Hautier, W. Chen, W. D. Richards, S. Dacek, S. Cholia, D. Gunter, D. Skinner, G. Ceder, and K. A. Persson, APL Mater. **1**, 011002 (2013).

[69] H. T. Stokes and D. M. Hatch, J. Appl. Crystallogr. **38**, 237 (2005).

[70] H. T. Stokes, D. M. Hatch, and B. J. Campbell., FINDSYM, ISOTROPY Software Suite, `iso.byu.edu` (2005).

[71] L. Wang, T. Maxisch, and G. Ceder, Oxidation energies of transition metal oxides within the GGA+U framework, Phys. Rev. B **73**, 195107 (2006).

[72] D. Kramer and G. Ceder, Tailoring the morphology of $licoo_2$: A first principles study, Chem. Mater. **21**, 3799 (2009).

[73] W. Sun and G. Ceder, Efficient creation and convergence of surface slabs, Surf. Sci. **617**, 53 (2013).